On the structural behaviour of a CFRP safety cage in a solar powered electric vehicle

Published Version:
Fragassa, C., Pavlovic, A., Minak, G. (2020). On the structural behaviour of a CFRP safety cage in a solar powered electric vehicle. COMPOSITE STRUCTURES, 252, 1-17 [10.1016/j.compstruct.2020.112698].

Availability:
This version is available at: https://hdl.handle.net/11585/768565 since: 2024-11-23

Published:
DOI: http://doi.org/10.1016/j.compstruct.2020.112698

Composite Structures 252 (2020) 112698

On the structural behaviour of a CFRP safety cage in a solar powered electric vehicle

Cristiano Fragassa, Ana Pavlovic [*], Giangiacomo Minak

Alma Mater Studiorum University of Bologna, Department of Industrial Engineering, via Fontanelle 40, 47121 Forlì, Italy

[*] Corresponding autho

E-mail addresses: cristiano.fragassa@unibo.it (C. Fragassa), ana.pavlovic@unibo.it (A. Pavlovic), giangiacomo.minak@unibo.it (G. Minak).

ABSTRACT

The use of composite structures represents a consolidated design strategy for solar race vehicles where weight savings can be immediately transformed into energy efficiency and, essentially, into better race performance. At the same time, no design assumption can sacrifice safety. This article describes the redesign of an existing solar prototype aimed at improving overall vehicle performance in terms of weight reduction and safety through replacement of titanium alloy with a CFRP carbon fiber reinforced laminate and sandwich structure as the main element of the vehicle safety system. Through appropriate optimization of materials, lay-up and sandwich structures it was possible to improve car safety while significantly reducing its weight.

1. Introduction

The development of solar vehicles has grown from an elementary design exercise performed by amateur sports enthusiasts [1–3] to a full-blown global challenge with a continually increasing number of universities, research centers and companies from all over the world taking part in design competitions, from Europe [4,5] to the Middle East [6], Asia [7], North America [8,9], South America [10], Africa [11] and Oceania [12]. Indeed, it is in the latter that the most important solar mobility event takes place every two years: the World Solar Challenge (WSC). This competition proposes the challenge of crossing Australia [13] from north to south, a 3022 km journey, using the Sun as the only source of energy [14]. It represents an extreme design requirement for solar vehicles that promotes the development of advanced engineering solutions specifically oriented to the efficient use of a small amount of available energy, equal to approximately 100kWh [15].

Energy savings and exploitation therefore represent key concepts that guide each choice in solar car development [16], from conceptual design [17] to race strategy [18]. It has been estimated that a 10% reduction in overall weight of an electric race vehicle can lead to a 13.7% energy saving [19].

Maximum energy efficiency in terms of vehicle design is sought through various strategies, such as optimization of aerodynamics [20–22], adjustment and balance of vehicle dynamics [23], elimination of kinematic friction [24], and strict optimization of manufacturing- ing processes [25]. Amongst others, one of the most highly regarded design strategies is weight minimization in order to reduce inertial mass and energy losses in non-conservative systems [26,27]. This design paradigm has commonly been achieved through the use of lightweight composite materials for both structural and non-structural vehicle parts, in particular thermoset resins reinforced with carbon fiber (CFRP) [28]. In [29], as well as many other investigations, the benefits of adopting reinforced composites for structural applications in vehicles are fully presented.

A wide-ranging assessment of material use and its impact on performance in the specific case of solar car design and manufacturing has been presented in [30], where several materials employed in current solar prototypes are considered. These vary from metals to composites, depending mainly on the team budget. A general increase in the tendency to use carbon fiber reinforcement for both solar vehicle structures and parts can be clearly noted worldwide and is related to the possibility of obtaining very light and stiff solutions.

In [31], for instance, the design and development of a solar car in Japan is described in which massive involvement of advanced composites took place. Made with ultra-lightweight carbon fiber fabric as thin as 0.06 mm, a 55 kg reduction in bodyweight was reported for a two- seater racing vehicle compared to a metal-based equivalent prototype. The study of extra lightweight vehicular structures for transport, including modeling of their behavior, are aspects that date back many years. In relation to solar vehicles, [32] proposes a model for supporting solar hybrid vehicle designers in accounting for aspects such as optimal sizing, dynamics, energy flow, cost, and weight. This work, together with many others [33], does not specifically address optimization of solar prototypes for competitive purposes but is intended to frame solar mobility in a broader context. The authors explore the multifaceted theme of automotive applications of solar energy [34], the promising nature of these technologies [35], and the potential benefit that solar and hybrid vehicles can offer in terms of energy savings and reductions in greenhouse gas emissions [36]. This can also be observed in [37], where an approach to modifying conventional vehicles, including structural design, is indicated as a way to obtain a more sustainable means of transportation.

Regardless of the motivation for minimizing weight through design, it is also strictly necessary to meet several functionality and safety criteria relating to the vehicles themselves. As reported in [38], lightweight vehicles of this type are formally categorized as light or heavy quadricycles, exhibiting specific risk profiles that are not fully accounted for in current legislation. These risk profiles should be carefully considered in the design approach, particularly in view of the high performance of existing prototypes that can reach speeds of >100 km/h [39].

Useful reviews of safety in automotive composite structural design are presented in [40,41]. Predominant aspects of design requirements are also presented in [42] in relation to the use of sandwich parts and in [43] in relation to impact loads.

Within this context, the present article reports the redesign of an existing solar prototype aimed at improving overall vehicle performance in terms of weight reduction and safety through the replacement of titanium alloy with CFRP. Though investigation into the strength of composite structures in automotive applications is certainly not new, with a large volume of excellent works in the literature [44,45], very few studies have directly focused on the design or rede- sign of solar-powered terrain vehicles [46,47] to the authors’ knowledge, while none have proposed a detailed example of the structural benefits achieved by substituting metallic materials with reinforced composite and sandwich structures.

2. Objectives

The core of this investigation centers around a solar-electric competition prototype [48] designed to run the American Solar Challenge (ASC) [49] in the *Multi-Occupant Vehicle* category (MOV) (Fig. 1).

This vehicle is categorized as a ‘heavy quadricycle’ accordingly to the *Le7CP* category of the 168/2013/EU standard, with a size of 4600x1800x1200mm and an empty weight (excluding batteries) of 230 kg. In the ASC race configuration, with a specific battery pack and four passengers on board, the vehicle exhibits a total weight of 700 kg.

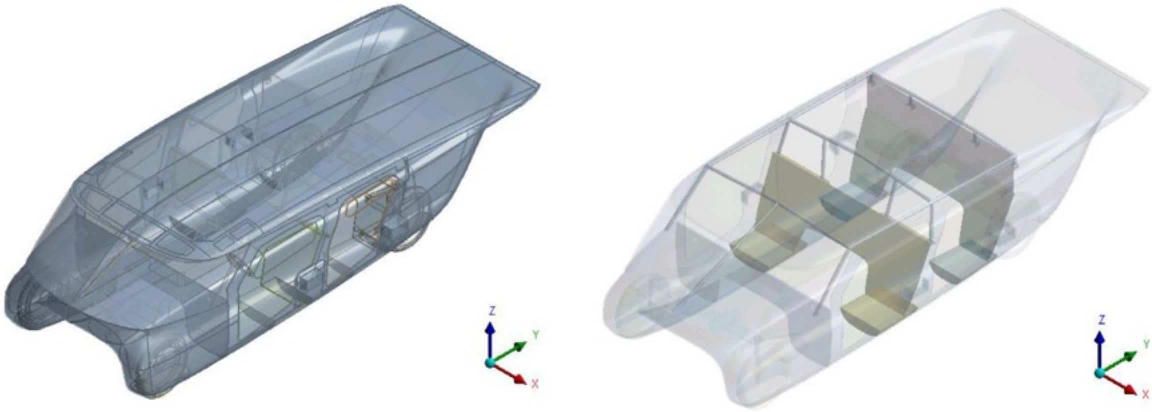

a)

b)

Fig. 1. The multi-occupant solar vehicle: a) overview of general layout (main parts transparent) and; b) detail of the metal roll bar.

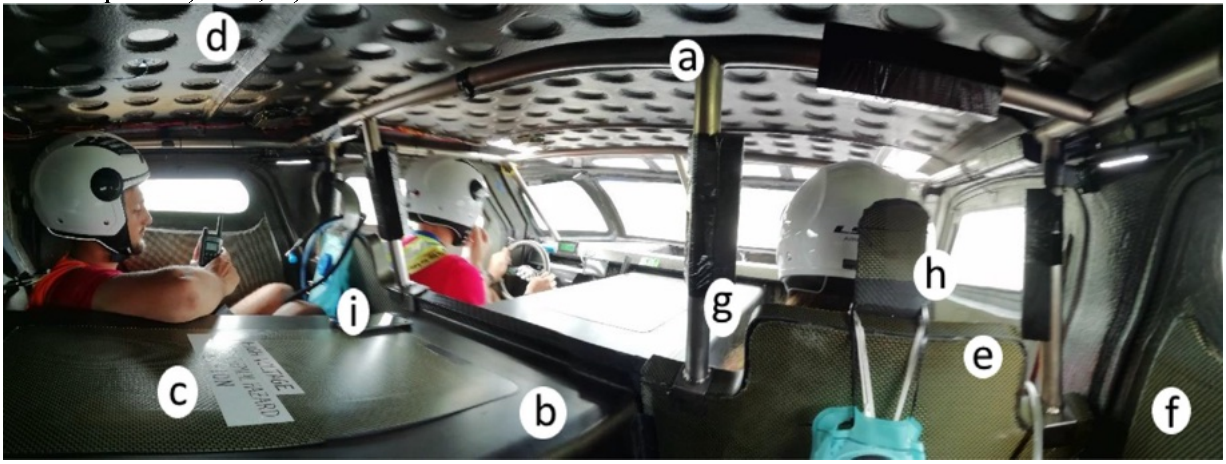

Fig. 2. Vehicle interior before design changes with: a) metal roll cage; b) battery pack access window; c) laminated central beam; d) sandwich-structure roof; e) seat; f) door, g) protective bumpers; h) headrest; i) water bottle.

This admirable result compared to similar prototypes was obtained through the extensive use of reinforced composite sandwich structures.

Although winner of the ASC 2018, covering a distance of 2780 km at an average speed of 55 km/h, this particular solar prototype did not meet the subsequent WSC 2019 regulations [50]; thus, a conceptual and structural redesign was required within which the new carbon structure was created.

The design process took place in line with new logic, taking into consideration the following requirements:

- the vehicle had to run a very different route with limited elevation change and a maximum altitude of 850 m;
- a cruising speed above 75 km/h was required to comply with regulations and, specifically, the presence of *time controlling gates*;
- the vehicle would use smaller and lighter solar panels to allow them to be moved and reconfigured by the driver alone;

- the vehicle required provision of safety structures able to resist higher loads compared to the existing metal roll cage.

These goals were approximately equivalent to doubling the range of an already extremely efficient vehicle. Therefore, it was necessary to intervene in a synergistic manner on many design aspects.

In terms of structural redesign, it was necessary to lighten the vehicle while safeguarding all other aspects such as functionality and safety. The possibility of replacing the metal roll bar with a composite solution was seen as an opportunity, as the former was no longer mandatory in the new regulations.

In practical terms, the structural intervention involved the design, optimization, and construction of a safety cage made of reinforced composite materials in place of the metal cage, able to withstand the stresses foreseen by race regulations in the event of car rollover.

A photo of the vehicle interior taken from the rear passenger side is presented in Fig. 2. The metal roll cage *(a)* required by previous reg- regulations is immediately visible. The metal tubes, no longer required under new regulations, are in clear contrast to other parts of the vehicles, which are made entirely of composite materials.

The hollow central beam *(b)* had the function of both containing the batteries and part of the electronics *(c)* while providing torsional stiffness. The roof *(d)*, also in CFRP, is clearly visible together with circular patterns for weight reduction. These sections, which represent holes in the support panel, not only reduced the weight of the structure but also helped dissipate heat. Photovoltaic panels, in fact, suffer rapid reductions in efficiency with temperature increases. Almost all of the sections described thus far were redesigned and modified as a consequence of the present work. The monocoque structure in which all elements are housed, comprising the central beam (battery holder) and lower bathtub structure (visible externally in Fig. 3) instead remained unchanged.

3. Methods

Replacement of the metal safety cage (Fig. 4a) was achieved by conceiving an alternative able to exploit the marked anisotropy of reinforced composites. Several options were considered, both in terms

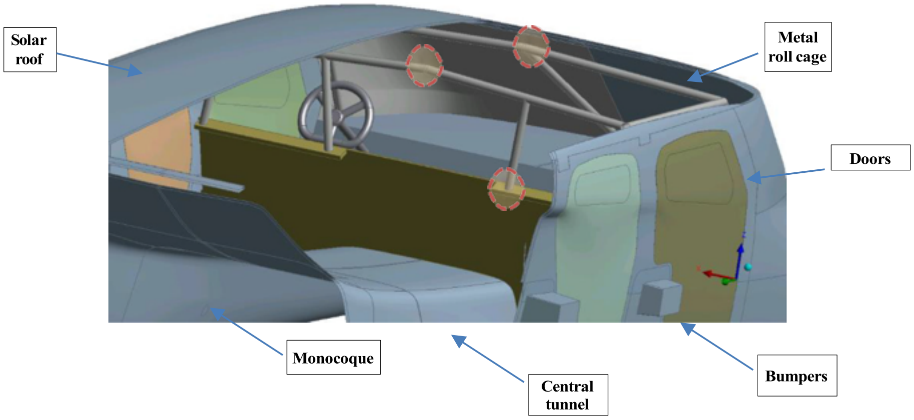

Fig. 3. External schematic of the vehicle. The metal roll cage is shown together with its critical zones.

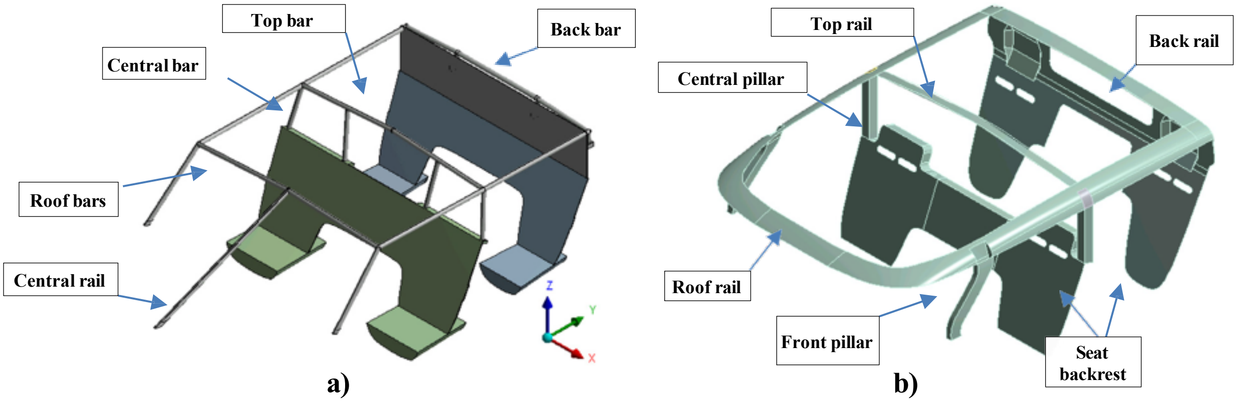

Fig. 4. Safety cage before and after redesign with all subsections: a) original metal roll-cage structure, as inserted in the composite structure (not visible); b) final structure in reinforced composite.

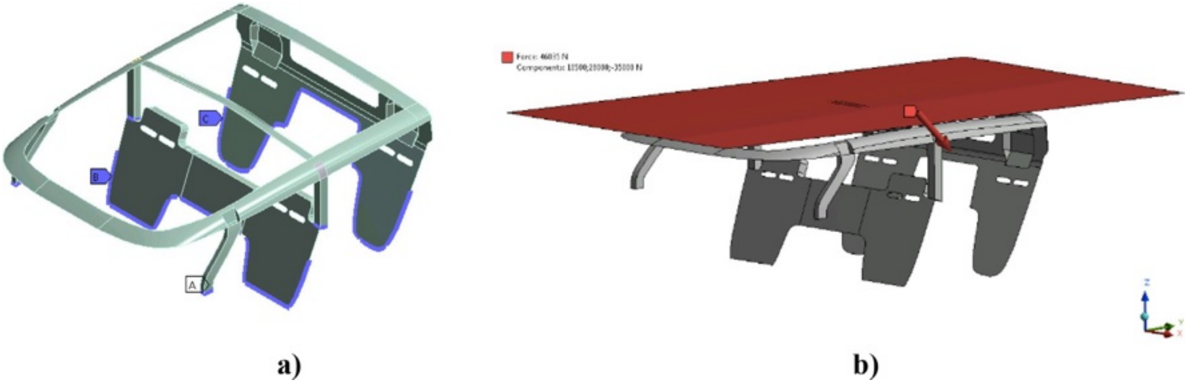

Fig. 5. Application of external conditions: (a) fixed constraints (in blue) on seat contours and pillar bases; b) applied load as a three directional force (46kN) transmitted by an infinitely rigid plate (in red).

of geometry and materials. The present discussion is limited the final solution (Fig. 4b).

The study was carried out considering the safety requirements defined within the WSC 2019 race regulations, comprising static analysis at pre-established loads and verification of maximum deformation. In particular, with the aim of protecting occupants from the potential risk of vehicle rollover, the regulation requires that a multi- directional load is applied in static conditions. This load must be equivalent to 5 times the weight of the vehicle in the vertical direction, 4 times in the longitudinal direction and 1.5 times in the transverse direction, applied to a section of the roof with a diameter smaller than 150 mm.

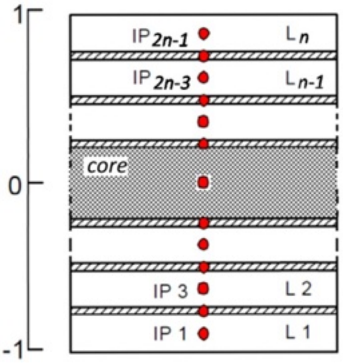

Fig. 6. Through-thickness integration points (IP) in an *n*-layer laminate with extra integration points at each interface for delamination prediction.

Physical conditions were reproduced with a finite element (FE) simulation using the commercial software ANSYS Workbench Ver.

18.2. A description of this modeling approach applied metal structures is presented in [51]. Numerical modeling was limited to the central and upper sections of the safety cage (Fig. 4b), in which the four seats also performed structural functions. These parts are rigidly anchored to underlying elements of the structure, specifically the monocoque and central tunnel, sections of the vehicle that can be considered infinitely rigid in relation to the applied external forces. The result is a simplified model with interlocking constraints where the seats and uprights are in contact with the vehicle (Fig. 5a).

A total weight of 750 kg was adopted for the investigation, including the mass of the frame, batteries, photovoltaic panels, engines, driver, passengers, and all other kinematic elements (e.g., wheels, suspension, etc.). This overall weight is higher than in the past due changes in the race configuration (larger battery pack, heavier engines, etc.), but also represents a more conservative approach to design validation.

The static loading system was applied by placing an infinitely rigid plate in contact with the roof of the vehicle. Given the geometry, the initial contact between the plate and structure only occurred within the central section of the middle safety cage roll bar. The plate was then loaded with a force in accordance with regulations in terms of magnitude and direction (Fig. 5b). Specifically, compression equivalent to 5 g downwards (Z direction), 4 g backwards (Y direction) and 1.5 g sidewards (X direction) was applied, with a resultant force of 46 kN.

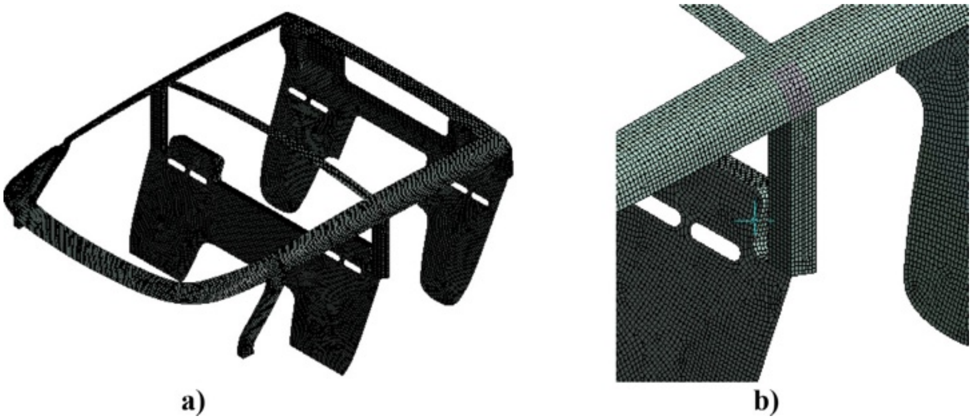

Fig. 7. Discretization of the geometric model using bidimensional (*shell181*) elements.

The choice of using a rigid obstacle (the plate) instead of directly applying forces to nodes was intended to provide better correspondence of loading conditions to the case of a real rollover. In particular, the plate allowed other sections of the structure, not engaged during initial contact, to be progressively included during impact progression and structure deformation. This effect was managed through control of the contact criteria between the surfaces.

The composite safety cage was discretized using a single-layer shell method, a common simplification when investigating macroscale phenomena in large structures or complex geometries. By correctly transforming properties, the multi-layered laminate could be considered equivalent to a single layer discretized with shell elements along the laminate surface and integration points (IPs) throughout the thickness [52]. One IP was employed per layer, providing accurate results for in- plane failures [52]. One IP was also employed per layer interface with the scope of considering out-of-plane phenomena such as delamination (Fig. 6). Discussion of this approach and comparison with alternatives is provided in [53,54], where a significant reduction in mesh complexity is reported, with good overall precision especially in detecting in-plane failures.

Two-dimensional (*shell*) elements with dimensions in the range 5–30 mm were used, with a total of 36,388 elements and 37,794 nodes (Fig. 7).

SHELL181 elements characterized by 4 nodes and 6 degrees of freedom (*dof*) per node were employed due to their suitability in applications where large rotations or large deformations emerge. Furthermore, *SHELL181* elements have also been shown to be appropriate in situations where layers must be discretized, as in the case of modeling composite shells or sandwich constructions [55–57].

Specifically, each lay-up was discretized by one specific FE layer. Convergence tests, carried out by progressively increasing the number of discretization layers and elements, exhibited stable outputs, with numerical results in terms of deformation changing by no >3% within the most sensitive areas. This discretization implied the use of FEs with a thickness of 0.15 or 0.30 mm in the presence of unidirectional or bidirectional fiber orientations, respectively.

4. Materials

Orthotropic material properties were introduced using the Ansys Composite PrePost (ACP) module in Ansys®. This allowed carefully definition of layering to be undertaken, attributing precise material characteristics to each layer including the orientation of fibers. Several configurations were defined based on the following (main properties given in Table 1):

Table 1
Fundamental material properties.

Property	Unit	T1000	T800
Type	–	*Unidirectional*	*Twill*
Density	Kg/m³	1490	1420
Young’s Modulus*	MPa	121000, 8600, 8600	61340, 61340, 6900
Poisson’s Ratio **	–	0.27, 0.4, 0.27	0.04, 0.3, 0.3
Shear Modulus **	MPa	4700, 3100, 4700	19500, 2700, 2700
Tensile Stress Limit *	MPa	2231, 29, 29	805, 805, 50
Compressive Stress Limit *	MPa	1082, 100, 100	509, 509, 170
Shear Stress Limit **	MPa	60, 32, 60	125, 65, 65
Tensile Strain Limit *	%	1.67, 0.32, 0.32	1.26, 1.26, 0.8
Compressive Strain Limit *	%	1.08, 1.92, 1.92	1.02, 1.02, 1.2
Shear Strain Limit **	%	1.2, 1.1, 1.1	2.2, 1.9, 1.9

** (X, Y, Z) directions; ** (XY, YZ, XZ) directions*

Properties	Unit	NOMEX	PVC	Ti Alloy
Type	–	*Honeycomb*	*Foam*	*Metal*
Density	Kg/m³	80	100	4620
Young’s Modulus	MPa	1, 1, 255	125	96,000
Poisson’s Ratio	–	0.49, 0.001, 0.001	0.40	0.36
Bulk Modulus	MPa	–	208	11,429
Shear Modulus	MPa	0, 37, 70	44	35,294
Tensile Yield Strength	MPa	–	2.5	930
Compressive Yield Strength	MPa	–	2.0	930
Tensile Ultimate Strength	MPa	0, 0, 5.31	2.5	1070

- T1000 and T800: high tensile strength carbon fibers manufactured by Toray, widely used for composite structures in automotive applications. Both T1000 and T800 are designed to meet requirements for lightweight structures, with the former representing one of the most resistant fibers available for conventional applications [58]. With different forms available on the market, pre-impregnated fabrics with 0.15 mm *unidirectional* T1000 and 0.3 mm *twill* T800 were employed.
- *Nomex:* the registered trademark of a *meta*-aramid-based substance developed by DuPont. From a chemical point of view, Nomex can be considered an aromatic nylon, the meta variant of Kevlar *para*-aramid. Produced analogously to paper, one of its various uses is to build honeycomb panels used in the construction of lightweight structures such as planes.
- Polyvinyl chloride (PVC): a thermoplastic obtained from natural raw materials presenting a versatile range of uses. It has good mechanical and chemical properties (e.g. wear, acid attack) for a lightweight

material.

A layer of carbon-Kevlar (supplied by Angeloni) was also present

on surfaces in contact with passengers (e.g. seats) to contain carbon chips in the event of cracks; however, this was not considered during structural optimization.

A realistic representation of material properties is one of the first problems faced by the designer of composite structures. Despite the use of commercial materials, the available datasheets are often inconclusive as constituent materials and processing conditions can deviate from specifications, with even slight changes significantly affecting the final properties.

In the present case, Toray declares proprieties for T800 and T1000 based on normalized values for a 60% Fiber Volume Ratio (FVR) and a specific epoxy resin and curing cycle [59]. These values can deviate significantly from those measured during experiments.

Results relating to T800H-12 k-50B have been reported [60], con- firming the fiber properties declared by Toray (tensile strength of 5.880GPa, tensile modulus of 294 GPa and elongation of 2.0% for a diameter of 5 μm) with only minor differences (tensile strength of 5.5GPa and elongation of 1.9%). The same cannot be said for fabric properties, with the four composites under consideration exhibiting tensile strengths between 2140 and 2680 MPa instead of the declared 3290 MPa, with similar variability found in relation to ILSS. Similar differences have also been confirmed in other studies [61], where the tensile strength was measured as between 1889 and 2220 MPa due to a different FVR, in line with the rule of mixtures (roughly 20%, ~720 MPa). In [62], where several reinforcements including Toray T1000 were compared, the FVR rarely passed 50% in the case of conventional unidirectional (UD) fabrics.

These considerations led to the use of conservative material proper- ties for the present safety validation, postponing the opportunity to improve accuracy via direct experimental characterization of the des- ignated reinforced materials to a later stage.

Table 2
Metal roll cage sections (made of Ti-alloy tubes with 30 mm diameter and 1.2 mm thickness).

Roll cage sections	N. of Parts	Length [mm]	Mass [kg]
central tube	1	1600	0.80
vertical central tube	4	400	0.80
side tube	2	1900	1.91
rear tube	1	1600	0.80
rear vertical tube	4	250	0.50
front tube	1	1600	0.80
vertical front tube	2	500	0.50
central front tube	1	1400	0.70
Overall*	16	13,600	6.82

** Those total values also consider the n. of parts*

Specifically, the Ansys database of composites was preferred (with values also in accordance with [63–66]) using material models *Epoxy Carbon Woven (230GPa) Prepreg* for T800S, *Twill*, K24000 and, conservatively, *Epoxy Carbon UD (230GPa) Prepreg* for T1000G, *Unidirec- tional*, K12000 in a *MTM49* epoxy resin system by *Solvay*. For *Nomex, PVC* and Titanium alloy, the *Ansys ACP* material models were selected as *HONEYCOMB (80 kg/m³)*, *PVC Foam (100 kg/m³)* and *Ti- alloy*, respectively. A summary of mechanical properties is reported in Table 1.

5. Metal structure

The pre-existing metal roll cage was also considered for comparison. Made of Ti-alloy with a density of 4620 kg/m^3, it consisted of a

13.6 m tube with 30 mm diameter and 1.2 mm thickness split into 16 segments of different lengths and welded, with an overall weight of 6.82 kg. Details are reported in Table 2.

The numerical simulation was performed in line with similar stud- ies performed by the authors for metal roll cages [67] using the load/- constraint conditions described above. *Shell 181* elements were also employed in this case, with 3431 nodes and 34,269 elements with dimension between 5 and 27 mm.

Fig. 8 exhibits the total and directional deformations for the metal roll cage. With a maximum displacement of 20.6 mm in the vertical (*Z)* direction, 27.2 mm longitudinally (*Y*) and 7.5 mm transversally (*Y*), the cage was deformed by 28.3 mm toward the passengers. As shown in Fig. 9, several zones enter the plastic regime (>930 MPa) or exceed the failure stress (>1070 MPa), with local Von Mises equivalent stresses exceeding 1500 MPa in some regions. Risk to the occupants in the case of a rollover is clear, providing the opportunity to adopt improvements in the design.

6. Composite structure

Manufacturing of the composite safety cage began with preparation of molds for the various subparts. The molds were manufactured by layup on models produced by CNC machining based on three-dimensional CAD representations of the various parts [48]. Models were produced in resins such as polyurethane foam [68] and in some cases wood-base materials such as MDF. Prior to pre-preg lamination, model surfaces were treated with chemical agents to facilitate subsequent removal of the molds. Similar surface treatments were also adopted for the molds. This precaution not only permitted easier release of parts after curing and a better surface finishing, but also reduced the risk of damaging molds during forming and extraction due to friction. On average, six surface treatments were performed on each surface.

Vacuum bags were prepared to apply mechanical pressure during curing. With a pressure of 1 bar, the scope of this step was to remove air trapped between layers, better compact the layers and remove moisture. The parts were then cured in an autoclave.

Full details of the process including applied pressures, the temporal temperature profile and other manufacturing parameters are discussed in [69]. In relation to the composite laminates, the pressure was set to 6 bar and the temperature increased at 2 °C/min up to 135 °C. Curing was performed under these conditions for 2 hrs before decreasing the temperature at 1 °C/min to room temperature. Special attention was paid to parts characterized by a sandwich structure to avoid excessive pressure or temperature that might damage the soft core (in *Nomex* or *PVC*). In particular, the maximum temperature was reduced to 125 °C and the pressure to 2.7 bar. Even under these conditions, the cores contracted by approximately 10%.

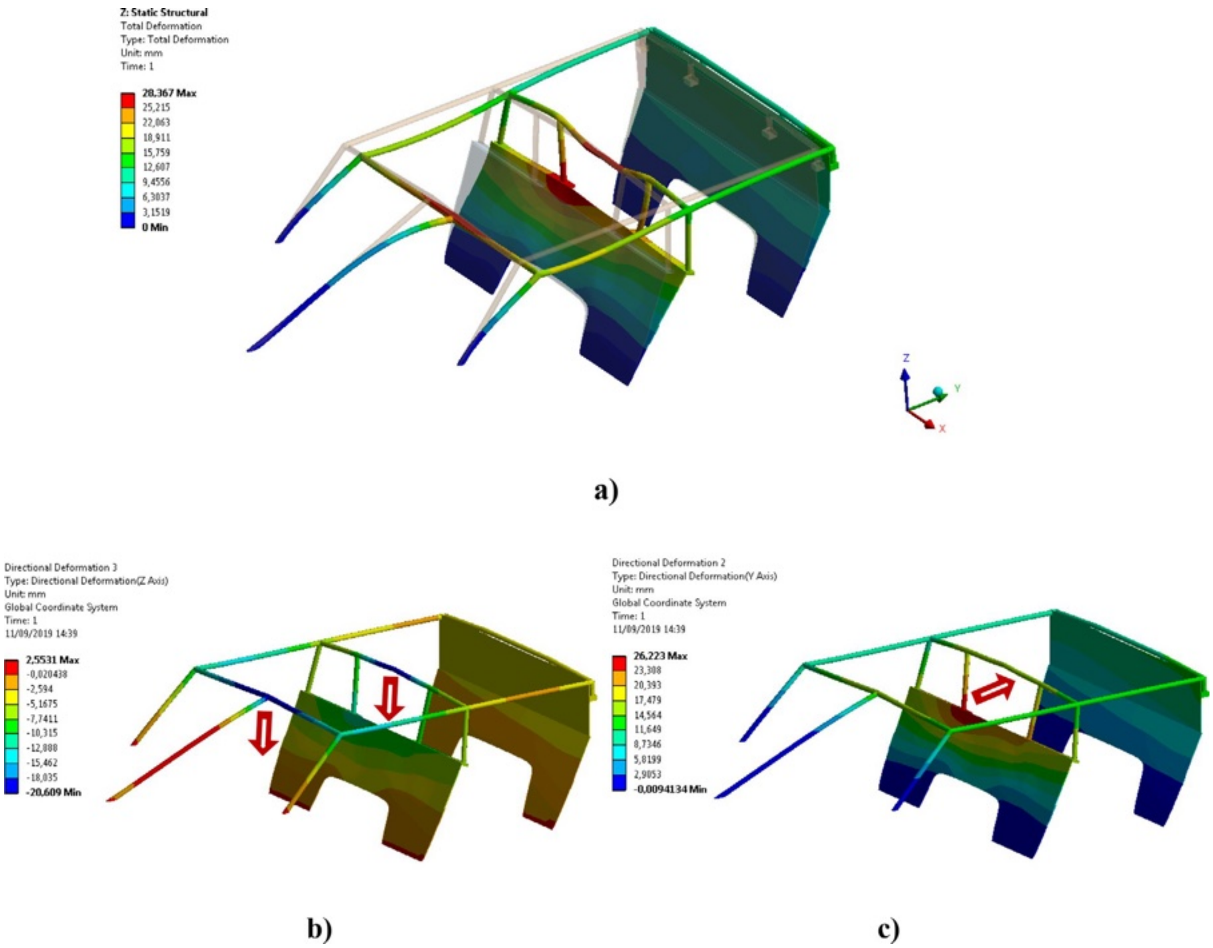

a)

b)

c)

Fig. 8. Total (a) and directional deformations in the case of a metal roll cage for: b) vertical (*z axis*) and c) longitudinal directions (*y axis*). Red arrows show the largest displacements (>20 mm) due to the rollover loads.

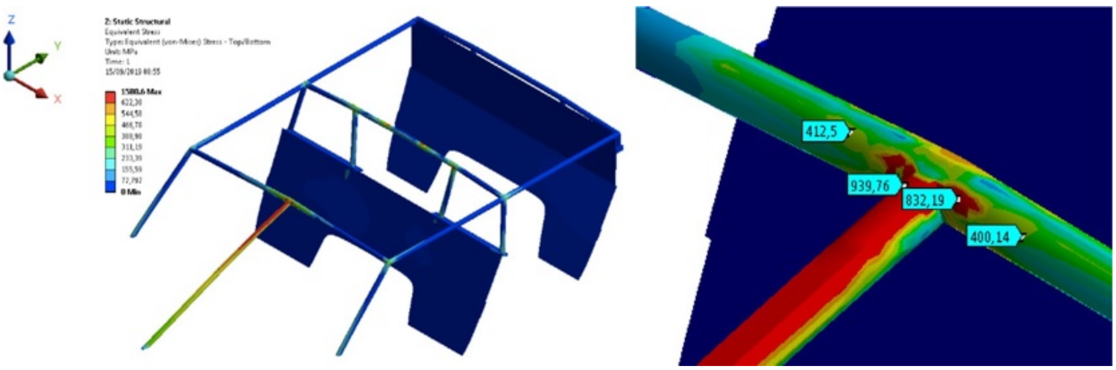

Fig. 9. Equivalent Von Misses stress in the case of a metal roll cage: a) entire structure and b) detail. Red areas represent zones where the stress level is close or higher than the Ti-alloy yield strength (930 MPa).

As noted previously, several lay-up variations were compared. All were defined in line with common guidelines for the design of composite structures such as:

- limit the number of layers as much as possible and, in particular, alternate between layers of different materials;
- ‘protect’ unidirectional (UD) layers (T1000), able to respond to the main directional loads, with woven layers (T800) on the surface, able to respond to loads from unexpected directions;
- superimpose no >4 layers of the same type
- use a sandwich structure with an inside core (in *Nomex* or *PVC*) as a design solution in the presence of flexural loads;
- arrange layers symmetrically about the center line to avoid bending or twisting during curing.

Table 3 describes the final lay-up configuration, reporting details relating to materials, thicknesses and deposition angles for each of the essential sections of the roll cage. In the case of T1000, a single layer of thickness 0.6 mm (at 0°) instead of 4 layers of thickness 0.15 mm is reported for simplicity. For instance, the *roof rail* component was obtained by laying up one layer of T800 *twill* with fibers at 0/90°, four thin layers of T1000 *UD* and one additional layer of T800 *twill* with fibers rotated at ±45°. The central core in *Nomex* was then positioned (Fig. 10) before performing the same lay-up in reverse order.

<Table 3
Final composite material layout.

Section	Front and Central Pillar			Top Rail			Back Rail			Roof rail and Seat Backrest		
Thickness	3.9 mm			4.8 mm			12.4 mm			12.4 mm		
Layers	Material Type	Thickness [mm]	Angle [°]	Material Type	Thickness [mm]	Angle [°]	Material Type	Thickness [mm]	Angle [°]	Material Type	Thickness [mm]	Angle [°]
1	T800	0.3	±45	T800	0.3	±45	T800	0.3	0/90	T800	0.3	0/90
2	T1000	4x0.15	0	T1000	4x0.15	0	T1000	4x0.15	0	T1000	4x0.15	0
3	T800	0.3	0/90	T800	0.3	0/90	T800	0.3	±45	T800	0.3	±45
4	T1000	4x0.15	0	T1000	4x0.15	0	*PVC*	10	0	*Nomex*	10	0
5	T800	0.3	0/90	T800	0.3	0/90	T800	0.3	±45	T800	0.3	±45
6	T1000	4x0.15	0	T1000	4x0.15	0	T1000	4x0.15	0	T1000	4x0.15	0
7	T800	0.3	0/90	T800	0.3	0/90	T800	0.3	0/90	T800	0.3	0/90
8	T1000	4x0.15	0	T1000	4x0.15	0						
9	T800	0.3	±45	T800	0.3	±45						
10				T1000	4x0.15	0						
11				T800	0.3	0/90						

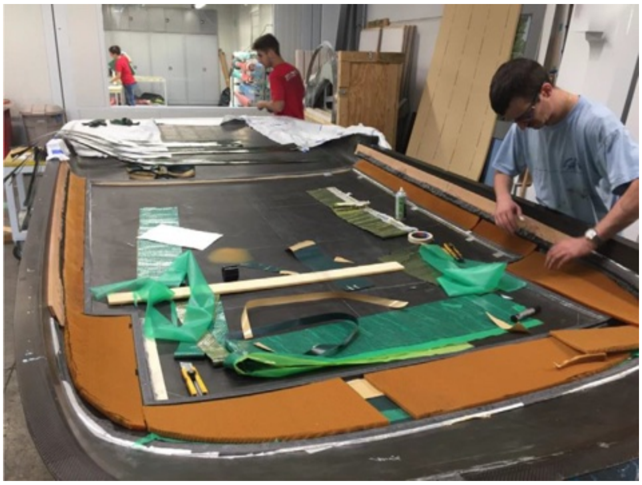

Fig. 10. Manufacturing of the composite sandwich structure. During lay-up of the roof rail, *Nomex* is positioned in the middle of the other layers.

Results

The total and directional deformation of the safety cage are presented in Fig. 11, where it is confirmed that the structure meets the safety criteria set by the regulations, which state that lowering of the roof must not exceed 25 mm. Maximum deformation in this direction (equivalent to the Z axis) is 24.9 mm, with this value obtained in sections near the doors where deformation does not interfere with the space occupied by the passengers. The simulation instead predicts that the central part of the roof lowers by <20 mm.

Fig. 12 provides an initial overview of the stress state, expressed in terms of the Maximum Principal Stress (MPS) averaged across all layers. This figure allows quick identification of the most critical zones, including the contact area between the plate and top rail

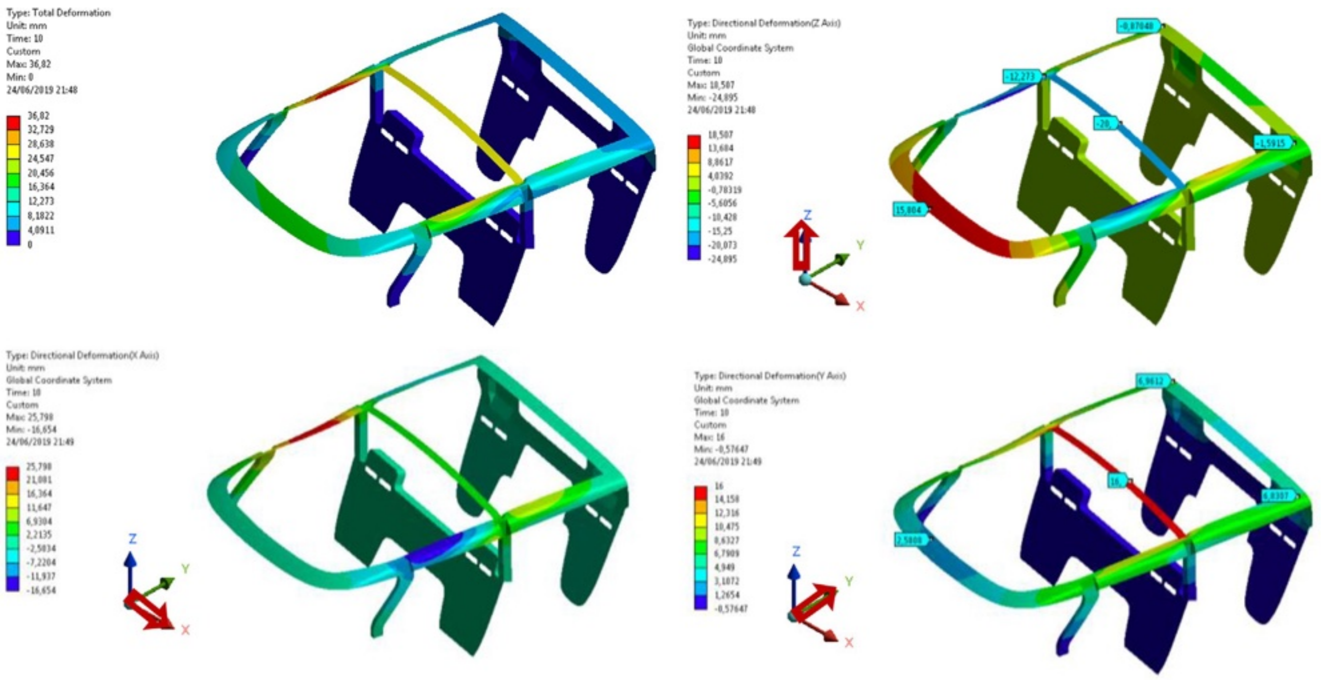

Fig. 11. Total and directional deformation of the CFRP roll cage.

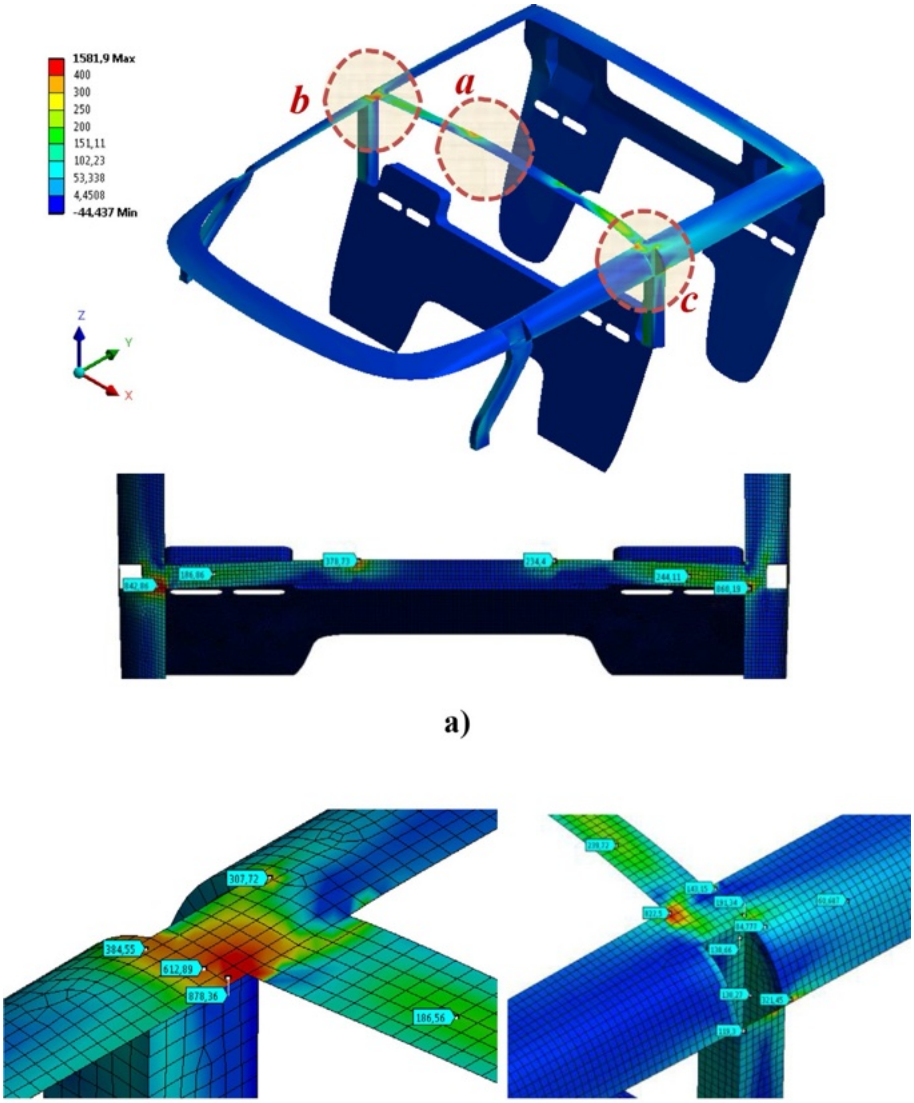

a)

b)

c)

Fig. 12. Maximum Principal Stress (MPS) in CFRP roll cage: overview and details of the most significant areas.

(Fig. 12a) and the two intersections between the central pillar, top rail and roof rail on both the driver (Fig. 12b) and passenger (Fig. 12c) sides of the vehicle. It must be noted that despite the symmetry of the structure and constraints with respect to a vertical *Y-Z* plane, the presence of an *X-component* (~22% of the total) of the external force leads to an asymmetrical stress state and deformation. Consequently, the *left* intersection is mostly subject to compressive stresses in the y-direction and the *right* to tensile stresses in the x- direction. The latter is less severe (~850 compared to ~1000 MPa) but also less critical in relation to material strength, which is higher under tensile loading than under compressive loading for CFRP (2231 compared to 1082 MPa for T1000). For the same reason, the zone with highest stress on the top rail is on the right (~380 compared to ~240 MPa) and shifted ~50 mm to the right with respect to the plane of symmetry (Fig. 12a).

Fig. 13 shows a distribution map of the MPS for each separate section of the most stressed layer. The highest value of MPS for each layer is reported in Table 4. The seats are not shown since they are subject to negligible stress under these test conditions.

Considering these values, the material stress limits for T800 or T1000 are not exceeded at any point. Principal stresses are useful for comparing metal and composite cages in the case of a rollover. In Fig. 14, the structural response of these structures in the above-mentioned conditions is represented in terms of von Mises equivalent stress for Ti-alloy and Maximum Princi- pal stress for CFRP.

In particular, the comparison highlights the fact that:

- the Ultimate Tensile Strength (UTS) of Ti-alloy (1030 MPa) is exceeded in several zones, implying structural failure. Large zones exceeding the plastic limit (>970 MPa) are also visible. On the contrary, in the case of CFRP, the maximum (principal) stress in the T1000 is much lower than the material UTS (~1000 MPa compared to 2200 MPa).
- even if the total deformation is comparable in both cases, with values in the range 20–30 mm, the metal roll bar exhibits dangerous deformation that is primarily in the *Y* direction, with 17–26 mm at the intersection between the central vertical bar and the front seat; practically at the back of the passenger.

Table 4
Highest value of the maximum principal stress for each layer.

Layer	Material Type	Front pillar	Central pillar	Top rail	Back rail	Roof Rail
1	T800	106	340	300	176	700
2	T1000	97	620	800	280	900
3	T800	120	370	525	190	700
4	T1000	102	600	900	0.5 *(PVC)*	3 *(Nomex)*
5	T800	97	365	445	38	222
6	T1000	107	577	750	70	1005
7	T800	75	357	427	40	271
8	T1000	112	555	809		
9	T800	76	256	460		
10	T1000			860		
11	T800			394		

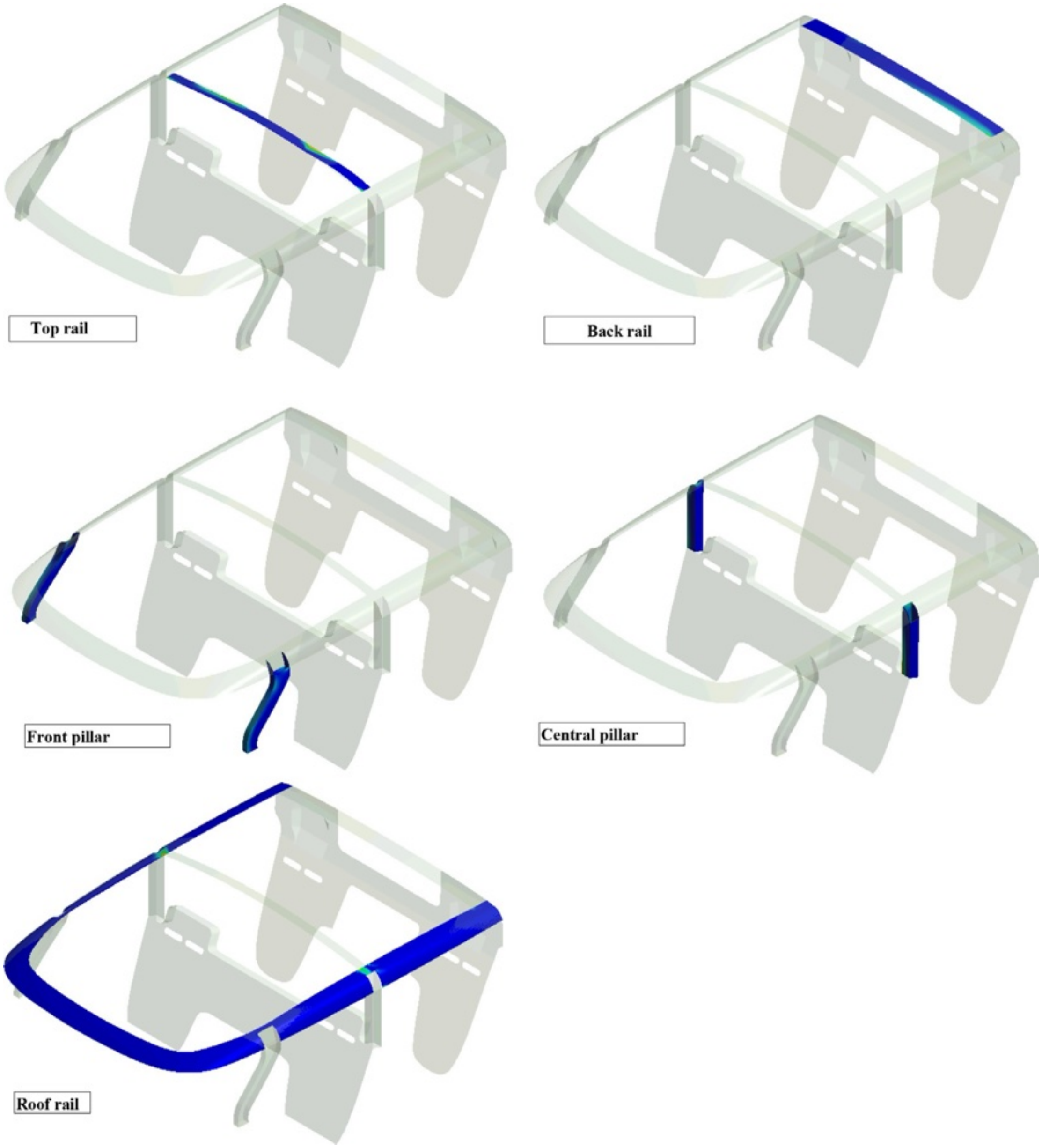

Fig. 13. Maximum principal stresses of the most stressed layer for each section.

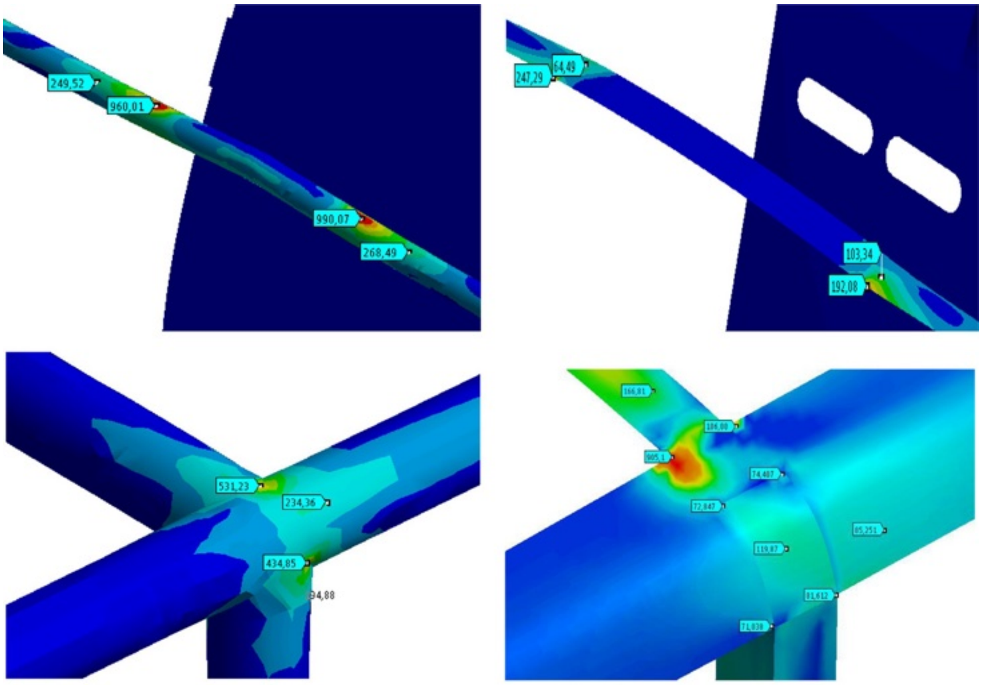

a) b)

Fig. 14. Comparison of stress values in the most critical zones for: a) metal (von Mises) and b) CFRP (Maximum Principal stresses).

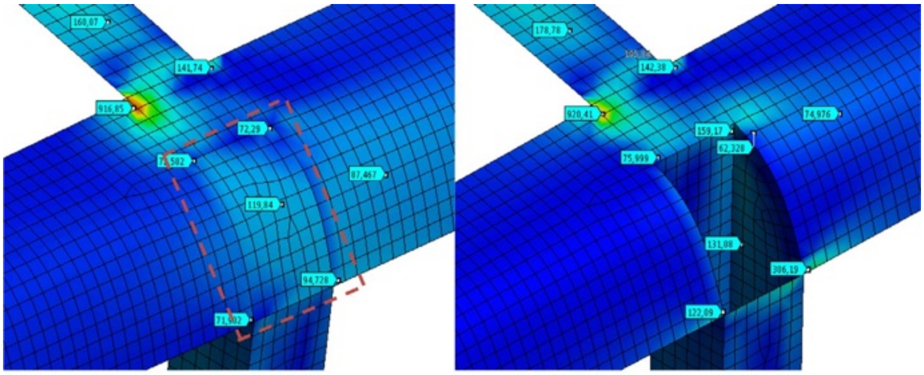

a) b)

Fig. 15. Effect of local changes in the geometry on maximum principal stresses.

This situation does not take place for the CFRP safety cage, where the higher stiffness of the central pillars and top rail compared to the tubular central and top bars, respectively, eliminates the requirement for vertical reinforcing elements joined to the front seats.

It must be noted that the numerical simulation was carried out with a slight modification to the real geometry. This difference, shown in Fig. 15, mainly relates to the absence of a roof rail segment over the central pillow. This 'window' was opened to allow better investigation into one of the most critically stress zones. This modification allowed some of the discontinuities present in the composite structure (i.e. the joining of three orthogonal composite elements) to be studied in greater detail.

7. Failure criteria

In terms of failure criteria, *ANSYS Workbench Ver. 18.2* provides *Maximum Stress*, *Maximum Strain,* and *Tsai-Wu Failure* as standard criteria [70,71]. While the first two are based on nine failure stresses or strains, respectively, Tsai-Wu also allows consideration of three additional coupling coefficients. Other commonly implemented criteria include *Tsai-Hill, Hoffman, Hashin, Puck, LaRC* and *Cuntze* [72]. These are physical failure criteria specifically formulated to account for different damage mechanisms, including fiber or matrix failure [73].

For each criterion, methods for estimating the probability of failure include the *Margin of Safety* (MoS), *Reserve Factor* (RF) and *Inverse Reserve Factor* (IRF), amongst others. The IRF, in particular, represents a dimensionless inverse margin to failure that is normalized against the load, where IRF > 1 means failure and IRF much lower than 1 (e.g. 0.5) means safety.

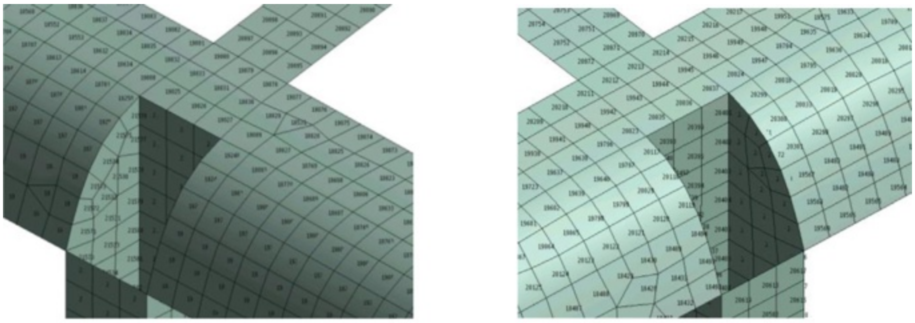
a) b)

Fig. 16. Discretization and element codes within the most relevant areas of interest.

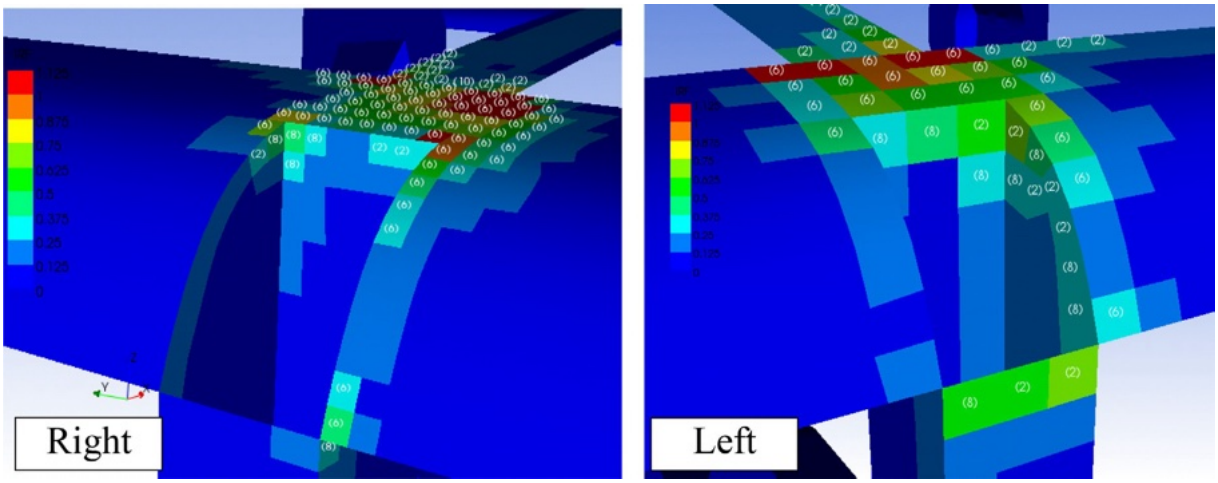

Fig. 17. Inverse Reserve Factor (IRF) map based on *Hashin* criterion. Layers with highest stress levels are reported in brackets.

As undertaken in the present study, each criterion must be considered separately for structural validation, as each can cause maximum IRF for different staking sequences.

Based on the numerically calculated stress states within the present study, the modeled composite structure met all safety requirements for each of the selected failure criteria (i.e. IRF < 0.50), with the exception of a single critical zone, the joint displayed in Fig. 15. Discretization and element codes for each FE within this zone are presented in Fig. 16.

For this preliminary analysis and discussion of results, the *Hashin* criterion was utilized. This condition takes into account matrix failure due to simultaneous axial and shear stress, allowing differentiation between fiber breakage, to be avoided, and matrix failure, which can be allowed as an extreme case in the event of overturning.

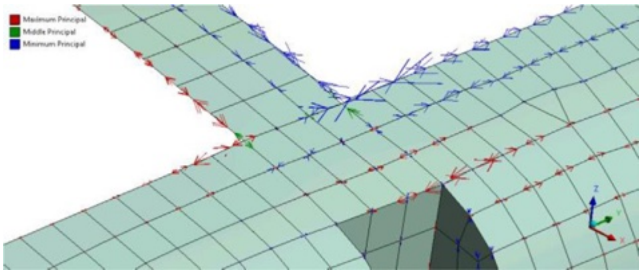

Fig. 18. Principal stress directions within 6th layer, corresponding to the fiber orientation in the UD composite.

Fig. 17 displays the IRF map based on the *Hashin* criterion. For each FE, the most stressed layer (highest IRF) is also reported in brackets. In the left section, all values are below 0.50 (corresponding to blue or green) except for six elements within the 6th layer of the roof rail, cor- responding to T1000 UD, where IRF > 0.875 (specifically, FE codes *20211, 20212, 20214, 20215* and *19944*). An additional element on the roof rail within the 6th layer and another on the top rail within the 2nd layer exhibit IRF values between 0.750 and 0.875 (specifically, FE codes *20970* and *19945*).

Fig. 18 exhibits further details relating to the 6th layer of the roof rail (T1000 UD), where it can be observed that the principal stresses are in the same direction as the fiber orientation (*x-axis*). Considering a fiber strength of 230GPa, it can be concluded that the IRF is primarily related to the failure of the matrix. The same situation takes place at the right intersection.

Combining different failure criteria, other elements emerge as being critical within the same region. All other parts of the safety cage do not exhibit criticalities (IRF < 0.750).

Fig. 19 presents the related IRF map for the left intersection, reporting the critical layer and corresponding criterion for each FE. Fig. 20 provides details distinguishing the criteria in question.

Without entering into detail, the failure criteria generally confirm that the structure is safe in all areas even if, under the defined loading conditions, failure could take place in one of the two intersections

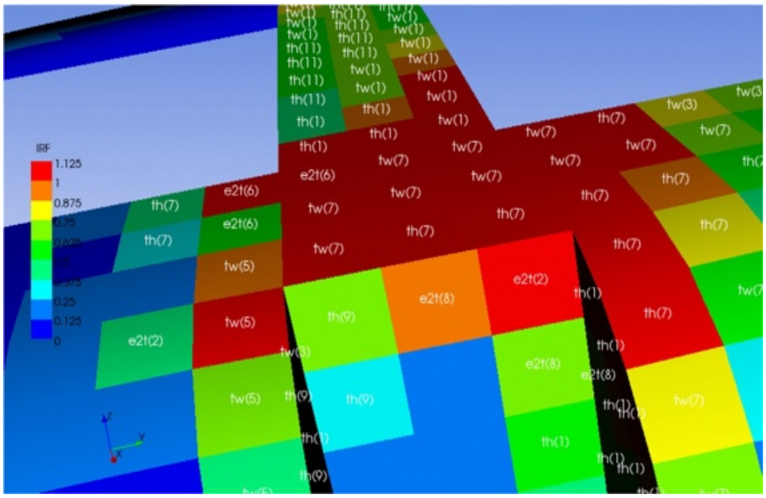

Fig. 19. Inverse Reserve Factor (IRF) map merging results from different failure criteria.

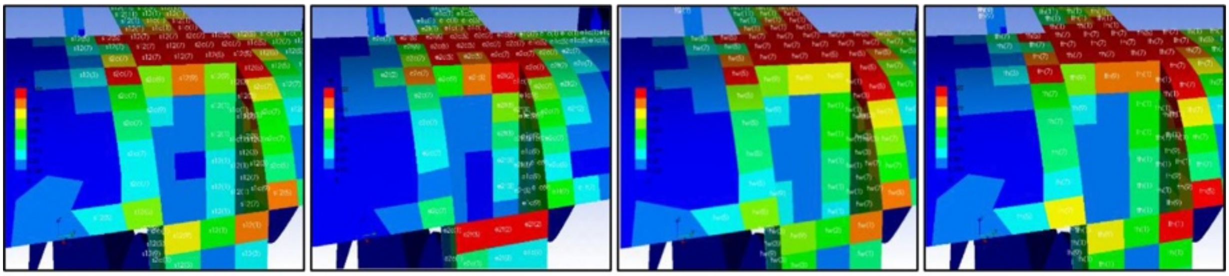

a) b) c) d)

Fig. 20. Inverse Reserve Factor (IRF) map for different failure criteria: a) Maximum Stress; b) Maximum Strain; c) Tsai-Wu; d) Tsai-Hill.

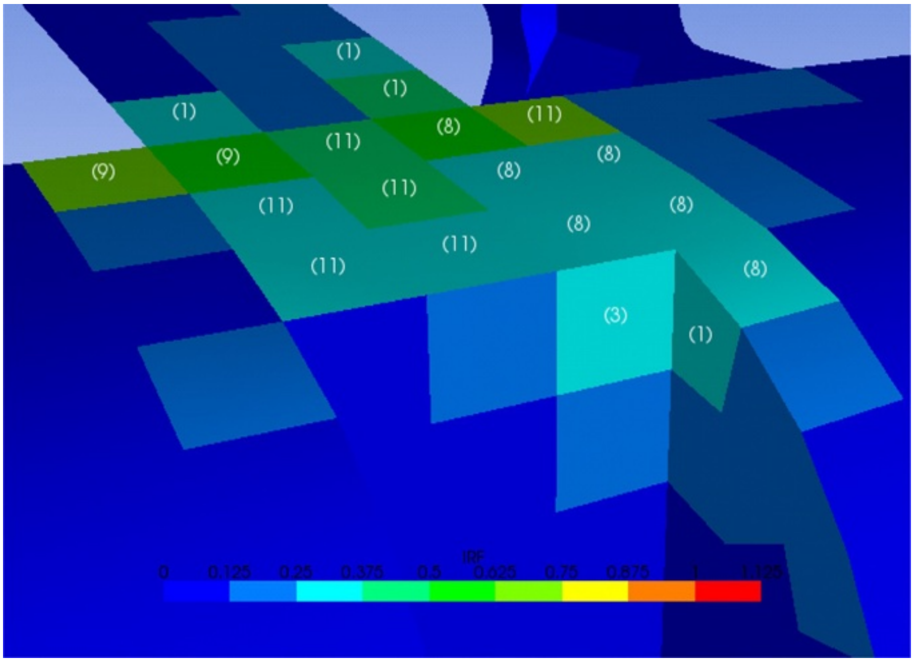

Fig. 21. Inverse Reserve Factor (IRF) for different failure criteria after local reinforcement.

Fig. 22. Layer-by-layer stress and material strength comparison in terms of IRF.

already identified (Fig. 12b and c). Although the stress states in these areas are generally oriented in such a way as to cause matrix failure, further reinforcement was nonetheless deemed appropriate. Given the need to contrast stresses in different directions to the principal ones, already supported by unidirectional fibers subject to stress well below their limit, reinforcement was performed using bidirectional layers (T800) and doubling T800 layers already present for approxi- mately 200 mm in all directions. For instance, the roof rail layout (de- tailed in Table 3) was modified locally by adding 4 layers of T800. As reported in Fig. 21, this design reduced the IRF values but also modify the critical layers.

8. Discussion

In-depth knowledge of the stress state of individual layers for ani- isotropic materials and the ability to account for different failure mechanisms (e.g., matrix or fiber failure) and different stress state directions leading to failure is a powerful tool for design optimization of composite structures. This is recognized by many authors [74,75] and is confirmed within the present study.

Stresses and strength are compared using IRF in Fig. 22. In regions where the IRF is low, the composite layout could potentially be modified in accordance with new design objectives where possible.

It can be observed how the upper layers (1–3) of the roof rail are less stressed than the rest. This circumstance would suggest the possibility of changing the sequence (i.e., removing a layer); however, this option is impractical as layer symmetry about the core must be maintained. It is therefore difficult to modify layers within the roof rail. Furthermore, special attention should be paid to the *Nomex* core as its integrity must be preserved since the material is quite weak and strongly anisotropic at a local level given the irregular geometry (similarly to details within [76]).

Fig. 23. Vehicle interior after design changes. The new composite structure eliminates all vertical metal bars inside the cockpit improving drivability and usability.

On the other hand, all other parts, including the front and central pillars and top and back rails, exhibit margin for changes, with the possibility of increasing stress and strain states to better exploit the material strength.

The IRF is very low for the front pillar and back rail, with regions that could benefit from layer changes (e.g. different pre-preg types or thicknesses).

Conceptual studies were performed with the numerical simulation to assess alternatives based on different goals.

In the case of weight reduction, layers of T800 with half the thickness were considered, leading to a 27% reduction in weight and a stress state in layers over the expected limits.

In view hypothetical vehicle commercialization, material selection could also be oriented towards less expensive composites. For instance, referring to the same type of pre-pregs and manufacturer, T1000 UD and T800 could be replaced, respectively, with T700 UD and T300, halving material costs.

The present research was limited to several conceptual evaluations for practical reasons, as optimization of costs was not strictly necessary for the competition prototype.

Furthermore, composite materials were readily available for proto-type construction, both in terms of type and quantity, allowing the structural layout detailed within this study to be constructed. This was desirable considering the fact that the entire safety of the four passengers was based on the composite structure. Ample safety margins beyond minimum requirements were therefore preferred in the structural design.

Technical decisions were also supported by the following considerations:

- the current race regulations offer specific conditions under which the vehicle must be certified (e.g. maximum vertical displacement in the case of a rollover). At the same time, new safety regulations may propose more stringent criteria that such a structure could reasonably respect without the need for significant changes;
- the regulation simplifies loading conditions relating to a road accident (e.g. frontal impact, side impact, rollover, etc.) by equating dynamic impact conditions to equivalent static loads (e.g. *n-times*

the vehicle’s weight in a certain direction). This approach appears overly simplistic and, while waiting to carry out crash studies, it was preferred to oversize the structure.

This form of overengineering does not simply refer to the use of a larger number of layers than was strictly necessary, but also to assumptions made during the study, such as the use of conservative values for material properties instead of values provided by the supplier.

The practical outcomes of replacing the metal roll cage with a composite structure are as follows:

- the composite structure meets all safety criteria;
- the roof could be modified and made more compact;
- the vertical bars present in the passenger compartment, between the seats and in the driver's line of sight, could be eliminated (Fig. 23);
- the drivability and usability of the vehicle could be improved.

9. Conclusions

The design of solar vehicles continues to challenge research groups from around the world to make continuous development key to their actions. This leads to the continuous evolution of such vehicles, with the best results exhibited every two years at the most important global solar car competition, the World Solar Challenge. This article details how the structure of an already competitive solar vehicle was modified to improve its performance and safety. The design strategy was based on changing the vehicle frame material from metal (titanium alloy) to fiber reinforced composite, allowing improvements in vehicle safety and a reduction in weight to be achieved. Though the new structure is heavier than the old one, 14 kg compared to 7 kg, such a comparison is not entirely fair. It must firstly be noted that the metal structure no longer satisfied updated design safety criteria, as stresses in the case of a rollover would have exceeded the ultimate strength of the material. This issue had not previously been taken into account due to different regulations in previous competitions.

The new CFRP cage also becomes part of the hood of the vehicle, lightening the roof as a whole. This integration between structural and non-structural parts in the composite roof also allowed other elements be lighten, in particular those locally supporting the solar cells, reducing the overall weight by roughly 15 kg.

It was also possible to remove the central rail located in the center of the windscreen, essential for correct functioning of the metal roll cage, to make the vehicle more drivable and functional. Finally, the composite safety cage allowed greater design flexibility with the possibility of reinforcing areas of greatest interest as required.

Declaration of Competing Interest

The authors declare that they have no known competing financial interests or personal relationships that could have appeared to influence the work reported in this paper.

Acknowledgements

Construction of the vehicle and its parts was carried out by members of *Onda Solare* Sports Association at the *MetalTig Srl* workshops (in Castel San Pietro Terme, Italy). Special recognition is dedicated to Mauro Sassatelli, Morena Falcone, Ruggero Malossi, Luigi Russi, Marco Bertoldi and Adrian Lutey.

Funding

This research has been carried out within the international collab- oration project '*Two Seats for a Solar Car*', an intervention funded by the *Italian* Ministry of Foreign Affairs and International Cooperation (MAECI), aimed at transforming a racing solar car into a solar road vehicle.

Appendix A. Supplementary data

Supplementary data to this article can be found online at https://doi.org/10.1016/j.compstruct.2020.112698.

References

[1] Wellington RP. Model solar vehicles provide motivation for school students. Sol Energy 1996;58(1–3):137–46.

[2] Carroll DR, Hirtz PD. Teaching multi-disciplinary design: solar car design. J Eng Educ 2002;91(2):245–8.

[3] McCartney G, Allen M, Cooper D, DeLissa L, Mayer E. Implementation of solar car technology 2019; Posters. 58. https://digitalcommons.pittstate.edu/posters_2019/58.

[4] Paterson G, Vijayaratnam P, Perera C, Doig G. Design and development of the Sunswift eVe solar vehicle: a record-breaking electric car. J Automob Eng 2016;230:1972–86.

[5] Ward J. Sun day drivers. Engineering 2007;248(10):75–7.

[6] Alnunu N, Said S, Al-Sharman, S, Al-Ibrahimi A, et al. Design of Qatar University's first solar car for Shell Eco-marathon competition. In: 2012 first international conference on renewable energies and vehicular technology. IEEE; p. 49–54.

[7] Suita Y, Tadakuma S. Driving performances of solar energy powered vehicle with novel maximum power tracking control for a solar car rally. In: 2006 IEEE international conference on industrial technology. IEEE; p. 1218–23.

[8] Mangu R, Prayaga K, Nadimpally B, Nicaise S. Design, development and optimization of highly efficient solar cars: Gato del Sol I-IV. In: 2010 IEEE green technologies conference. IEEE; p. 1–6.

[9] King RJ. Solar cars race for the future results of the GM Sunrayce USA and the world solar challenge. Sol cells 1991;31(5):395–424.

[10] Betancur E, Mejía-Gutiérrez R, Osorio-Gómez G, Arbelaez A. Design of structural parts for a racing solar car. In: Advances on mechanics, design engineering and manufacturing. Springer, Cham; p. 25–32.

[11] Menasce D, Grobler M, van Rensburg PJ. High power electrical systems design for a solar car: designing and building the solar car IlangaI. In: 2013 Africon. IEEE; p. 1–5.

[12] Lovatt HC, Ramsden VS, Mecrow BC. Design of an in-wheel motor for a solar- powered electric vehicle. IEE Proc-Electric Power Applications 1998;145 (5):402–8.

[13] Slezak M. Solar-powered cars streak across Australia in 3000km race. NewScientist 2013;220(2939):19–20.

[14] Green MA. Event Report. Brain sport: the 1996 world solar challenge solar car race across Australia. Progr Photovoltaics: Res Applications 1997;5(1):69–76.

[15] Thacher EF. A solar car primer, a guide to the design and construction of solar- powered racing vehicles. Springer; 2015.

[16] Hilliard A, Jamieson GA. Winning solar races with interface design. Ergonomics Design 2008;16(2):6–11.

[17] Watkins S, Humphris C. Solar vehicles: the challenge of maximum speed from minimal power. In:

ASME 2002 joint US-European fluids engineering division conference. ASME Digital Collection; p. 1009–14.

[18] Shimizu Y, Komatsu Y, Torii M, Takamuro M. Solar car cruising strategy and its supporting system. JSAE Rev 1998;19(2):143–9.

[19] Joost W. Reducing vehicle weight and improving U.S. energy efficiency using integrated computational materials engineering. J Miner Metals Mater Soc 2012;64:1032–8.

[20] Kin WD, Kruger S, van Rensburg NJ, Pretorius L. Numerical assessment of aerodynamic properties of a solar vehicle. In: Proceeding of the ASME international mechanical engineering congress and exposition, San Diego (US); 2013.

[21] de Kock JP, van Rensburg NJ, Kruger S, Laubscher RF. Aerodynamic optimization in a lightweight solar vehicle design. In: Proceeding of the of ASME international mechanical engineering congress and exposition, Montreal (Canada); 2017, p. 1–8.

[22] Ozawa H, Nishikawa S, Higashida D. Development of aerodynamics for a solar race car. JSAE Rev 1998;19:343–9.

[23] Odabasi V, Maglio S, Martini A, Sorrentino S. Static stress analysis of suspension systems for a solar-powered car. FME Trans 2019;47(1):70–5.

[24] Holmberg K, Andersson P, Erdemir A. Global energy consumption due to friction in passenger cars. Tribol Int 2012;47:221–34.

[25] Betancur E, Fragassa C, Coy J, Hincapie S, Osorio G. Aerodynamic effects of manufacturing tolerances on a solar car. In: Proceeding of the international conference on sustainable design and manufacturing, Bologna (Italy); 2017, p. 868–76.

[26] Joost W. Reducing vehicle weight and improving U.S. energy efficiency using integrated computational materials engineering. J Miner Metals Mater Soc 2012;64:1032–8.

[27] Wennhage P. Weight minimization of sandwich panels with acoustic and mechanical constraints. J Sandwich Struct Mater 2001;3(1):22–49.

[28] Brooks R, Brown KA, Warrior NA, Kulandaivel PP. Predictive modeling of the impact response of thermoplastic composite sandwich structures. J Sandwich Struct Mater 2010;12(4):449–76.

[29] Beardmore P, Johnson CF. The potential for composites in structural automotive applications. Compos Sci Technol 1986;26(4):251–81.

[30] Minak G, Fragassa C, de Camargo FV. A brief review on determinant aspects in energy efficient solar car design and manufacturing. In: International conference on sustainable design and manufacturing, Bologna (Italy), Springer; 2017, p. 847–56.

[31] Tamura S. Teijin's advanced carbon fiber technology used to build a car for the World Solar Challenge. Reinf Plast 2016;60(3):160–3.

[32] Arsie I, Rizzo G, Sorrentino M. A model for the optimal design of a hybrid solar vehicle. Review of automotive engineering. Soc Automotive Eng Japan (JSAE) 2008;29(3):439–47.

[33] Quaschning V. Technology fundamentals - the sun as an energy resource. Renew Energy World 2003;6(5):90–3.

[34] Rizzo G. Automotive applications of solar energy. IFAC Proc Vol 2010;43 (7):174–85.

[35] Connors J. On the subject of solar vehicles and the benefits of the technology. In 2007 international conference on clean electrical power. IEEE; (2007, May), p. 700–5.

[36] Kulkarni S, Edwards DJ, Parn EA, Chapman C, Aigbavboa CO, Cornish R. Evaluation of vehicle lightweighting to reduce greenhouse gas emissions with focus on magnesium substitution. J Eng Design Technol 2018;16(6):869–88.

[37] Rizzo G, Naddeo M, Pisanti C. Upgrading conventional cars to solar hybrid vehicles. Int J Powertrains 2018;7(1–3):249–80.

[38] Pavlovic A, Fragassa C. General considerations on regulations and safety requirements for quadricycles. Int J Qual Res 2015;9(4):657–74.

[39] Trottemant E, Nuna II. Breaks all records to win the world solar challenge. E. S. A. Bull 2003;116:52–3.

[40] Kollar LP, Springer GS. Mechanics of composite structures. Cambridge University Press; 2003.

[41] Gay D. Composite materials: design and applications. CRC Press; 2014.

[42] Zenkert D. An introduction to sandwich construction. Sheffield, UK: Engineering Materials Advisory Services Ltd; 1995.

[43] Abrate S. Impact on composite structures. Cambridge University Press; 2005.

[44] Zhu G, Sun G, Li G, Cheng A, Li Q. Modeling for CFRP structures subjected to quasi-static crushing. Compos Struct 2018;184:41–55.

[45] Feraboli P, Masini A, Taraborrelli L, Pivetti A. Integrated development of CFRP structures for a topless high performance vehicle. Compos Struct 2007;78 (4):495–506.

[46] Ning H, Janowski GM, Vaidya UK, Husman G. Thermoplastic sandwich structure design and manufacturing for the body panel of mass transit vehicle. Compos Struct 2007;80(1):82–91.

[47] Liu Q, Lin Y, Zong Z, Sun G, Li Q. Lightweight design of carbon twill weave fabric composite body structure for electric vehicle. Compos Struct 2013;97:231–8.

[48] Minak G, Brugo TM, Fragassa C, Pavlovic A, De Camargo FV, Zavatta N. Structural design and manufacturing of a cruiser class solar vehicle. J Visual Experiments 2019;n:143.

[49] American Solar Challenge, 2018 Regulations - Revision B http://americansolarchallenge.org/ASC/wp-content/uploads/2017/09/ASC2018-Regs- External-Revision-B.pdf (accessed on 01.06.2018).

[50] World Solar Challenge, 2019 Regulations, https://www.worldsolarchallenge.org/ event-information/2019_regulations (accessed 30.06.2019)

[51] Sharma V, Purohit D. Simulation of an off-road vehicle roll cage a static analysis. Simulation 2012;24:126–8.

[52] Rajbhandari SP, Scott ML, Thomson RS, Hachenberg D. An approach to modelling and predicting impact damage in composite structures. In: ICAS congress; September 2002, p. 8–13.

[53] Bogenfeld R, Kreikemeier J, Wille T. Review and benchmark study on the analysis of low-velocity impact on composite laminates. Eng Fail Anal 2018;86:72–99.

[54] Szekrényes A. Analytical solution of some delamination scenarios in thick structural sandwich plates. J Sandwich Struct Mater 2019;21(4):1271–315.

[55] Coelho PG, Guedes JM, Rodrigues HC. Multiscale topology optimization of bi- material laminated composite structures. Compos Struct 2015;132:495–505.

[56] Dhurvey P, Mittal ND. Finite element analysis of internally ply drop-off composite laminates. Int J Eng Res 2012;1(1):12–6.

[57] Pawar, Utpat A. Analysis of composite laminate for maximum stiffness. Int J Recent Technol Eng (IJRTE) 2014;3(2):60–6.

[58] Chae HG, Newcomb BA, Gulgunje PV, Liu Y, Gupta KK, et al. High strength and high modulus carbon fibers. Carbon 2015;93:81–7.

[59] Toray: Type of Composite Fibers. https://www.toraycma.com/page.php?id=661. (access on 20.03.2020).

[60] Zhang Q, Liang S, Sui G, Yang X. Influence of matrix modulus on the mechanical and interfacial properties of carbon fiber filament wound composites. RSC Adv 2015;5(32):25208–14.

[61] Chen W, Yu Y, Li P, Wang C, Zhou T, Yang X. Effect of new epoxy matrix for T800 carbon fiber/epoxy filament wound composites. Compos Sci Technol 2007;67:2261–70.

[62] Czél G, Jalalvand M, Wisnom MR. Design and characterisation of advanced pseudo-ductile

unidirectional thin-ply carbon/epoxy–glass/epoxy hybrid composites. Compos Struct 2016;143:362–70.

[63] Sai Ashok M, Koteswara Rao U. Failure analysis of unidirectional composite pinned-joints. Int J Eng Dev Res 2017;5(4):139–47.

[64] Ramkuvar NV, Mankar RL. Weight optimisation of wind mill shaft by composite material using FEA. Int J Adv Res Innov Ideas Educ 2017;3(4):138–45.

[65] Ullah H, Harland AR, Silberschmidt VV. Dynamic bending behaviour of woven composites for sports products: experiments and damage analysis. Mater Design 2015;88:149–56.

[66] Toygar ME, Tee KF, Maleki FK, Balaban AC. Experimental, analytical and numerical study of mechanical properties and fracture energy for composite sandwich beams. J Sandwich Struct Mater 2019;21(3):1167–89.

[67] Pavlovic A, Zivkovic M. Roll cage design and validation for a rally vehicle. FME Trans 2016;444:398–404.

[68] Fragassa C, de Camargo VF, Giorgini L. Quality assessment of carbon fiber automotive parts when using polyurethane foam as pattern material. In: AIP conference proceedings, Vol. 1981, No. 1, 17–22 June 2018, Ischia (Italy). No, 020088; doi:10.1063/1.5045950. AIP Publishing LLC.

[69] Sodena PD, Kaddourb AS, Hinton MJ. Recommendations for designers and researchers resulting from the world-wide failure exercise. Compos Sci Technol 2004;64:589–604.

[70] Hashin Z. Failure criteria for unidirectional fiber composites. J Appl Mech 1980;47 (2):329–34.

[71] ACP User's Guide, Ansys Inc., Canonsburg (PA), US; 2019.

[72] Mastrogiannakis I, Vosniakos GC. Exploring structural design of Francis Hydro- Turbine Blades Using Composite Materials. Facta Universitatis Ser: Mech Eng 2020. https://doi.org/10.22190/FUME190609001M.

[73] Barbero EJ. Finite element analysis of composite materials using ANSYS. CRC Press; 2013.

[74] Lee D, Morillo C, Bugeda G, Oller S, Oñate E. Multilayered composite structure design optimisation using distributed/parallel multi-objective evolutionary algorithms. Compos Struct 2012;94(3):1087–96.

[75] Pohlak M, Majak J, Karjust K, Kuttner R. Multi-criteria optimization of large composite parts. Compos Struct 2010;92(9):2146–52.

[76] Ha GX, Zehn MW, Fragassa C, Marinkovic D. Dealing with nap-core sandwich composites: how to predict the effect of the symmetry. Materials 2019;12(6):874.